

Particles-on-Demand for Kinetic Theory

B. Dorschner,^{*} F. Bösch, and I. V. Karlin[†]

Department of Mechanical and Process Engineering, ETH Zurich, 8092 Zurich, Switzerland

(Dated: February 27, 2022)

A novel formulation of fluid dynamics as a kinetic theory with tailored, on-demand constructed particles removes any restrictions on Mach number and temperature as compared to its predecessors, the lattice Boltzmann methods and their modifications. In the new kinetic theory, discrete particles are determined by a rigorous limit process which avoids ad hoc assumptions about their velocities. Classical benchmarks for incompressible and compressible flows demonstrate that the proposed discrete-particles kinetic theory opens up an unprecedented wide domain of applications for computational fluid dynamics.

Kinetic theory of Boltzmann and Maxwell, as the fundamental link between particles' picture of flowing matter and a continuum projection thereof, has been a valuable source of ideas in fluid dynamics. This especially concerns the lattice Boltzmann method (LBM) [1–4], a modern approach to the simulation of complex flows. LBM is a recast of fluid mechanics into a kinetic theory for the populations of designer particles $f_i(\mathbf{x}, t)$, with simple rules of propagation on a space-filling lattice formed by discrete speeds $\mathcal{C} = \{\mathbf{c}_i, i = 1, \dots, Q\}$, in discrete-time t , and relaxation to a local equilibrium $f_i^{\text{eq}}(\mathbf{x}, t)$ at the nodes \mathbf{x} . LBM witnessed burgeoning growth in applications and becomes the method of choice for complex fluid dynamics problems such as turbulence [5], wetting-dewetting transition [6], microfluidics [7, 8], microemulsions [9] and hemodynamics [10], to mention a few; recent reviews can be found in [11–13].

However, a critical look at LBM reveals major limitations: all practical LBM models are severely restricted in flow speed and temperature range. While these restrictions may be traded for deeply subsonic, slow flows, even then insufficient isotropy and lack of Galilean invariance impede simulations [14]. Moreover, the said limitations become eventually insurmountable for compressible flows [15–19]. It may be argued that LBM has reached its natural limits with the simulation of quasi-incompressible flows, and a different discrete kinetic theory is needed for important fields such as combustion and aerodynamics. In this Letter, we demonstrate that eventually all physical limitations of the LBM are removed once the discrete kinetic theory is formulated using tailored rather than fixed particles' velocities at every space location and every time instance. The new fully explicit realization outperforms LBM by many orders in terms of flow speed and temperature. This opens door to kinetics-based simulations of fluid dynamics which were not possible before. We begin with a clarification: LBM interprets the discrete speeds \mathbf{c}_i as particles' velocities, $\mathbf{v}_i^{\text{L}} = \mathbf{c}_i$. On the contrary, here we understand \mathbf{c}_i as *peculiar velocities* [20],

relative to a reference frame velocity \mathbf{u} and a temperature T . Henceforth, particles' velocities are defined as

$$\mathbf{v}_i = \sqrt{\theta} \mathbf{c}_i + \mathbf{u}, \quad (1)$$

where $\theta = T/T_L$ is the temperature reduced by the lattice temperature T_L , a constant which is known for any set of discrete speeds \mathcal{C} [21]. According to (1), LBM amounts to setting a global reference frame “at rest,” $\mathbf{u} = \mathbf{0}$, and choosing the fixed temperature $T = T_L$ for all particles. Here, we rather follow the interpretation (1) where the reference frame velocity and temperature are kept so far undetermined, and we are going to find optimal values for \mathbf{u} and T , as presented in detail below.

By specifying the frame velocity and temperature in (1), one sets the reference frame (or gauge) $\lambda = \{\mathbf{u}, T\}$ for the discrete velocities. LBM corresponds to the standard gauge $\lambda_L = \{\mathbf{0}, T_L\}$. We denote $f^\lambda = (f_1^\lambda, \dots, f_Q^\lambda)^\dagger$ as the vector of populations relative to the gauge λ . The transform of the populations to another gauge $\lambda' = \{\mathbf{u}', T'\}$ is facilitated by matching Q linearly independent moments (m, n are integers; $D = 2$ to ease notation),

$$M_{mn}^\lambda = \sum_{i=1}^Q f_i^\lambda (\sqrt{\theta} \mathbf{c}_{ix} + u_x)^m (\sqrt{\theta} \mathbf{c}_{iy} + u_y)^n. \quad (2)$$

Let us use a short-hand notation for a linear map of populations into moments M^λ (2), $M^\lambda = \mathcal{M}_\lambda f^\lambda$, where \mathcal{M}_λ is the $Q \times Q$ matrix of the linear map. The matching condition for the moments in both gauges λ and λ' reads,

$$M^\lambda = M^{\lambda'}. \quad (3)$$

In other words, the moments of the populations are independent of the choice of a gauge. Moments matching condition (3) implies that populations are transformed from one gauge to another with the transfer matrix $\mathcal{G}_\lambda^{\lambda'}$,

$$f^{\lambda'} = \mathcal{G}_\lambda^{\lambda'} f^\lambda = \mathcal{M}_{\lambda'}^{-1} \mathcal{M}_\lambda f^\lambda. \quad (4)$$

Finally, we introduce a reconstruction formula for populations at any point \mathbf{x} at time t :

$$\tilde{f}^\lambda(\mathbf{x}, t) = \sum_{s=1}^k a_s(\mathbf{x} - \mathbf{x}_s) \mathcal{G}_{\lambda_s}^\lambda f^{\lambda_s}(\mathbf{x}_s, t), \quad (5)$$

^{*} Present address: California Institute of Technology, Pasadena, CA 91125, USA

[†] Corresponding author; karlin@lav.mavt.ethz.ch

where $\lambda_s = \{\mathbf{u}(\mathbf{x}_s, t), T(\mathbf{x}_s, t)\}$ are the gauges at the collocation points \mathbf{x}_s , at time t , and a_s are interpolation functions (standard Lagrange polynomials below; k determines the order). Note that the reconstruction formula (5) enforces populations at collocation points to be treated in a specified gauge λ through the transform (4). We now present the discrete kinetic theory in an optimal local gauge. Introducing the time step δt , evaluation of the populations at the monitoring point \mathbf{x} at time t involves the propagation and the collision steps, mediated by the gauge transform.

Propagation. Semi-Lagrangian advection is performed first, using the reconstruction formula (5) at the departure point of characteristic lines, $\mathbf{x} - \mathbf{v}_i^0 \delta t$,

$$f_i^{\lambda_0} = \tilde{f}_i^{\lambda_0}(\mathbf{x} - \mathbf{v}_i^0 \delta t, t - \delta t), \quad (6)$$

where the characteristic directions \mathbf{v}_i^0 (or discrete velocities, cf. Eq. (1)) are set relative to a seed gauge $\lambda_0 = \{\mathbf{u}_0, T_0\}$. For the latter, it is convenient to choose flow velocity and temperature at the monitoring point \mathbf{x} at time $t - \delta t$:

$$\mathbf{u}_0 = \mathbf{u}(\mathbf{x}, t - \delta t), \quad (7)$$

$$T_0 = T(\mathbf{x}, t - \delta t), \quad (8)$$

yielding

$$\mathbf{v}_i^0 = \sqrt{\theta_0} \mathbf{c}_i + \mathbf{u}_0, \quad (9)$$

with $\theta_0 = T_0/T_L$. Since \mathbf{u}_0 and T_0 are known from the previous time step, the populations (6) are determined unambiguously in this *predictor* propagation step.

With the populations (6), the density, momentum and temperature are evaluated at the monitoring point using discrete velocities (9):

$$\rho_1 = \sum_{i=1}^Q f_i^{\lambda_0}, \quad (10)$$

$$\rho_1 \mathbf{u}_1 = \sum_{i=1}^Q \mathbf{v}_i^0 f_i^{\lambda_0}, \quad (11)$$

$$D\rho_1 T_1 + \rho_1 \|\mathbf{u}_1\|^2 = \sum_{i=1}^Q \|\mathbf{v}_i^0\|^2 f_i^{\lambda_0}. \quad (12)$$

This defines the *corrector* gauge $\lambda_1 = \{\mathbf{u}_1, T_1\}$ at the monitoring point, and advection (6) is executed anew with the updated velocities, $\mathbf{v}_i^1 = \sqrt{\theta_1} \mathbf{c}_i + \mathbf{u}_1$, to get corrected post-propagation populations $f_i^{\lambda_1}$. The predictor-corrector process is iterated until convergence, with the limit values,

$$\rho(\mathbf{x}, t) = \lim_{n \rightarrow \infty} \rho_n, \quad (13)$$

$$\mathbf{u}(\mathbf{x}, t) = \lim_{n \rightarrow \infty} \mathbf{u}_n, \quad (14)$$

$$T(\mathbf{x}, t) = \lim_{n \rightarrow \infty} T_n, \quad (15)$$

$$f_i^{\lambda(\mathbf{x}, t)} = \lim_{n \rightarrow \infty} f_i^{\lambda_n}, \quad (16)$$

defining the density (13), the flow velocity (14), the temperature (15) and the pre-collision populations (16) at the monitoring point \mathbf{x} at time t . Note that, by construction, the limit gauge $\lambda(\mathbf{x}, t) = \{\mathbf{u}(\mathbf{x}, t), T(\mathbf{x}, t)\}$ is the co-moving reference frame in which the discrete particle's velocity (1) is defined by the values of the flow velocity and of the temperature at the monitoring point.

Collision: In the co-moving reference frame, the local equilibrium populations are defined by the density only,

$$f_i^{\text{eq}} = \rho W_i, \quad (17)$$

where the weights W_i are known for any discrete speeds set \mathcal{C} [21], see also Appendix A. [Note that, in the standard LBM context, populations (17) would be identified as local equilibrium “at zero flow velocity $\mathbf{u} = \mathbf{0}$ ”.] Hence, pre-collision populations (16) are transformed to post-collision as

$$f_i(\mathbf{x}, t) = f_i^{\lambda(\mathbf{x}, t)} + 2\beta \left[\rho(\mathbf{x}, t) W_i - f_i^{\lambda(\mathbf{x}, t)} \right], \quad (18)$$

for the Bhatnagar-Gross-Krook (BGK) collision model. The relaxation parameter β is related to the kinematic viscosity by $\nu = T(1/2\beta - 1/2)\delta t$. By fixing the temperature and canceling the energy corrections (12), one arrives at the isothermal version of the proposed kinetic theory. Comments are in order here:

(i) In LBM, particles (represented by discrete velocities) are fixed once and for all with the identification $\mathbf{v}_i^L = \mathbf{c}_i$. Then the local equilibrium acquires non-invariant dependence on the flow velocity and temperature which leads to errors once $\mathbf{u} \neq \mathbf{0}$ and $T \neq T_L$. Accumulation of these errors is also the primary source of numerical instabilities when the plain BGK collision model is used in LBM. On the contrary, the new representation of kinetics creates “optimal particles” (or optimal discrete velocities), specific to each monitoring point at a given time (see propagation step) so that the equilibrium (17) “seen” by the populations becomes *exact*. Hence, this new representation is, in principle, restricted neither in the flow speed nor in the range of temperature variation. Error-free equilibrium can also result in unconditional numerical stability when using the BGK model. Below, we shall probe all this with benchmark simulations.

(ii) If the standard gauge λ_L is adopted, then the transfer matrix \mathcal{G} is dropped in (5), and advection (6) becomes $f_i = \tilde{f}_i(\mathbf{x} - \mathbf{c}_i \delta t, t - \delta t)$. The latter, together with finite element reconstruction, was used in a recent semi-Lagrangian LBM (SLLBM) [22]. SLLBM is not restricted to space-filling lattices and was realized on body-fitted unstructured meshes [23], an obvious advantage if turbulent flow simulations are concerned. Present algorithm fully retains this crucial feature.

The standard two-dimensional nine-speeds set *D2Q9* was used in all simulations below and the BGK collision (18) was implemented for both isothermal and compressible flow. The transfer matrix was found in closed form and is presented in Appendix B, together with the reconstruction formula realization. The LBM time step $\delta t = 1$ was used in all simulations.

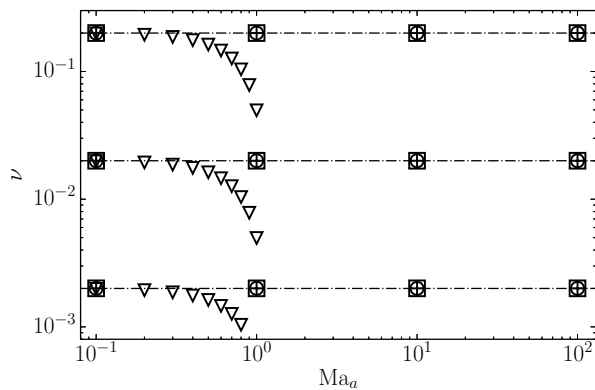


FIG. 1. Kinematic viscosity from decaying $\pi/4$ -tilted shear wave with $D2Q9$, at various advection Mach numbers $Ma_a = u/\sqrt{T}$. Lattice temperature $T_L = 1/3$. Lines: imposed theoretical values $\nu = 0.2$, $\nu = 0.02$, $\nu = 0.002$; Symbol: present method at fixed temperature $T_L/2$ (cross), T_L (circle) and $2T_L$ (square); Triangle: LBGK [4] at T_L .

First, we measured kinematic viscosity at isothermal conditions. The decay of plane shear wave with initial profile $u_x(\xi, \eta) = A \sin(2\pi\xi/L)$, $A = 0.05$, in transverse direction and advection $u_y(\xi, \eta) = Ma_a \sqrt{T}$ in the wave-vector (longitudinal) direction was studied. The wave vector was rotated by $\pi/4$ with respect to the standard Cartesian x -axis and periodic boundary conditions were applied in both longitudinal and transverse directions. This tilted-wave setup is standard to probe isotropy and Galilean invariance [24, 25]: kinematic viscosity should not depend on the advection Mach number Ma_a . An equidistant mesh with resolution $L = 200\sqrt{2}$ in longitudinal direction was used. Kinematic viscosity was measured by least square fit of exponentially decaying function. In Fig. 1, the kinematic viscosity is shown for various temperatures, in a wide range of advection speeds. It is apparent that the results of the present formulation are in excellent agreement with theoretical prediction, for advection Mach numbers even as high as $Ma_a = 100$, and are independent of temperature. This is in sharp contrast to the standard lattice BGK (LBGK) [4] which shows lack of Galilean invariance already at $Ma_a \gtrsim 0.1$. While the latter failure of LBM has been long known [24, 25], it is striking that a mere reformulation of the *same* kinetic model in the optimal gauge extends validity by at least three orders of magnitude in terms of flow speed. Note that, since the temperature can be set at a high value, and not only at $T = T_L$ as in the LBM, the quasi-incompressible flow simulations can be performed at realistic Mach numbers with the present method. This was used in the Green-Taylor vortex simulation at $Ma \sim 10^{-3}$ which confirmed second-order convergence, see Appendix D.

We now turn to the compressible flow while still using the nine-speeds $D2Q9$. The difference with the above isothermal model is that now the energy conservation

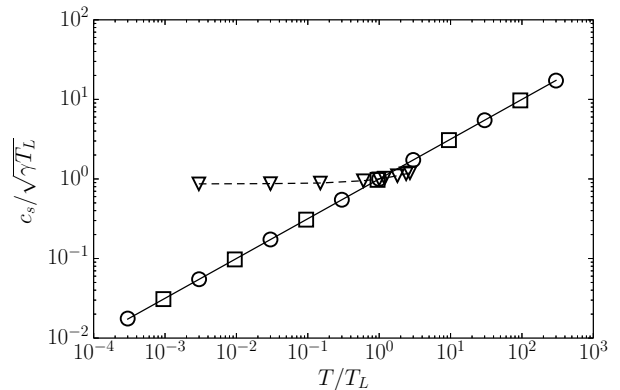


FIG. 2. Speed of sound with $D2Q9$. Line: theory, $c_s = \sqrt{2T}$; Circle: present method without advection; Square: present method with an advection Mach number $Ma_a = 10$. Triangle: thermal LBGK [26].

(12) is included in the predictor-corrector propagation step of the algorithm. The LBM counterpart is the thermal LBGK [27]. The first numerical experiment concerns measuring the speed of sound and comparing it to the theoretical prediction, $c_s = \sqrt{\gamma T}$, where the adiabatic exponent $\gamma = 2$ for two-dimensional ideal gas. To that end, speed of sound was measured by introducing a pressure disturbance $\Delta p = 10^{-3}$ and tracking the resulting shock front. Results for a fluid at rest, and advected with $Ma_a = 10$ are presented in Fig. 2. It is apparent that the speed of sound measured in the simulation excellently agrees with theory for all temperatures in the range $T \in [10^{-4}, 10^2]$, irrespectively of the advection speed. Fig. 2 also shows that the thermal LBGK with nine speeds matches the correct speed of sound only *at* the lattice temperature $T = T_L$ [26]. Thus, the present method extends the physical relevance of thermal LBGK by about six decades in terms of temperature range. We further probe the conduction of heat by measuring thermal diffusivity from the decay of a sinusoidal temperature profile [28]. A periodic set-up is chosen with an initial density $\rho = A \sin(2\pi x/L) + \rho_0$ at constant pressure $p = \rho_0 T_L$, with amplitude $A = 0.001$, $\rho_0 = 1$ and longitudinal resolution $L = 300$. Theoretical prediction of thermal diffusivity for the $D2Q9$ model is $\alpha = (T/4)(1/2\beta - 1/2)\delta t$ [26]. Fig. 3 demonstrates excellent agreement between theory and numerical results, for a range of advection speed up to $Ma_a = 100$, whereas thermal LBGK [27] shows severe deviations.

In general, simulations of compressible flows with LBM require higher-order lattices, with a much larger number of discrete speeds [29–32]. We conclude this Letter by comparing the above nine-speeds $D2Q9$ model with the entropic LBM on a higher-order lattice with forty-nine speeds, $D2Q49$ [29]. The benchmark consists of the advection of a vortex by a uniform flow. The vortex with radius R is propagated with advection Mach number $Ma_a = U_\infty/\sqrt{2T_\infty}$ while the vortex Mach num-

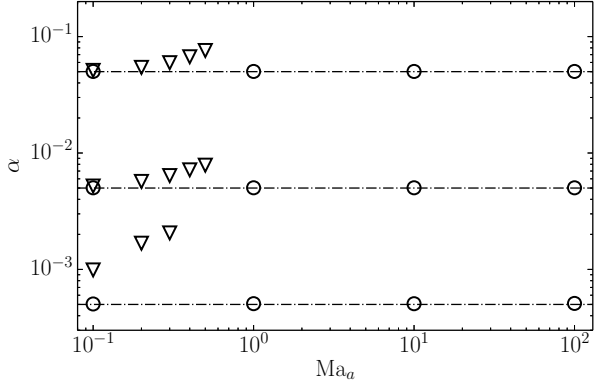


FIG. 3. Thermal diffusivity with $D2Q9$ lattice at various advection Mach numbers $Ma_a = u/\sqrt{2T}$. Line: theory; Circle: present method; Triangle: thermal LBGK [26, 27].

ber Ma_v defines the tangential velocity of the vortex $u_\varphi(r) = Ma_v r \exp[(1 - r^2)/2]$, where $r = r'/R$ is the reduced radius [33, 34]. In Fig. 4, pressure contours are shown for the present $D2Q9$ model (top row), together with those computed by the entropic LBM $D2Q49$ [29] (bottom row), for various combinations of Ma_a and Ma_v . Note that LBM [29] is in a global gauge $\lambda = \{\mathbf{U}, T_L\}$, $\mathbf{U} = (1, 0)$; this minimizes errors whenever $u_x \sim 1$. Clearly, with a global gauge conveniently chosen, unidirectional advection at small vortex Mach numbers can be accomplished with LBM (Fig. 4, first column). However, deviations of the local velocity and temperature away from the global gauge eventually lead to spurious deformation of the vortex (Fig. 4, second and third column). In contrast, present method shows no deformation of the propagating vortex, even for large Mach numbers (Fig. 4, last column). This shows superiority of the present method over the higher-order LBM.

Other pertinent aspects were studied using this benchmark. We observed that the predictor-corrector tailoring of the particles required about two to three iterations to convergence, with maximum of five at a fraction of grid points, when the gauge was initialized as in (7,8); see Appendix E. Independence of the limit from the seed gauge was probed by choosing different values of \mathbf{u}_0 and T_0 ; for example $\mathbf{u}_0 = \mathbf{0}$, $T_0 = T_L$, or even “unnatural” $\mathbf{u}_0 = -\mathbf{u}(\mathbf{x}, t - \delta t)$. We found that converged values are independent of the initialization which reveals that flow density, velocity and temperature are indeed defined correctly by the limits (13), (14) and (15).

Thus, we can view the particles as an attractor of the predictor-corrector process. Basin of attractor depends on the Mach number and narrows down at larger values; however, the seed gauge (7,8) was always included in the basin. This shows robustness of emerging kinetic picture.

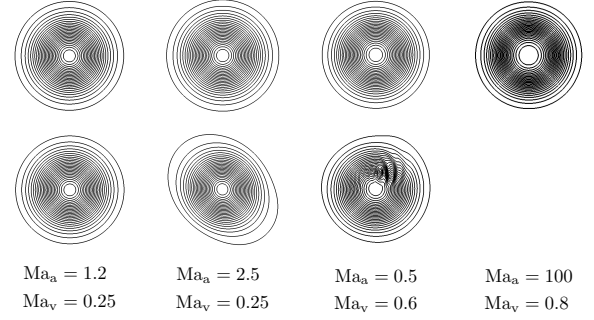


FIG. 4. Pressure contours of the vortex propagation for various advection and vortex Mach numbers. Top row: present method, $D2Q9$; Bottom row: entropic LBGK, $D2Q49$ [29].

Summarizing, the LBM is rigorously valid in the limit of vanishing flow velocity and at fixed lattice temperature. Practitioners of LBM circumvent these limitations by setting empirical bounds on the allowed variation of velocity and temperature (e. g., the flow velocity to stay below ten percent of the lattice speed of sound, $\|\mathbf{u}\| \lesssim 0.1\sqrt{T_L}$, a common recommendation for incompressible flow simulations; see Fig. 1). However, such heuristic constraints cannot be universally maintained and quickly become meaningless especially for compressible flows.

In this Letter, we proposed a major revision of the kinetic theory for fluid dynamics by constructing “particles-on-demand” instead of a priori fixed. Its realization demonstrates that the range of accessible flow velocities and temperatures becomes eventually unlimited. Same as in the LBM, the collision step retains locality and makes application of advanced collision models, already elaborated in LBM, straightforward in the present context, e. g. for varying Prandtl number and adiabatic exponent. The new discrete kinetic theory necessarily abandons the LBM lattice propagation since tailoring particles’ velocities does not match to the links of a lattice. While the propagation step becomes computationally more intensive than in LBM, the algorithm is still fully explicit, and, as our simulations show, the net demand is lower than that of the higher-order LBM while the operation domain is incomparably larger. Finally, error-free collision results in outstanding numerical stability even with the simplest BGK model. This all, as we believe, opens up an entirely new perspective on complex flow simulations.

This work was supported by the SNF grants P2EZP2.178436 (B.D.) and 200021-172640 (F.B.), and the ETH research grant ETH-13 17-1. Computational resources at the Swiss National Super Computing Center (CSCS) were provided under the grant s800.

-
- [1] U. Frisch, B. Hasslacher, and Y. Pomeau, Phys. Rev. Lett. **56**, 1505 (1986).
- [2] G. R. McNamara and G. Zanetti, Phys. Rev. Lett. **61**, 2332 (1988).
- [3] F. J. Higuera, S. Succi, and R. Benzi, Europhys. Lett. **9**, 345 (1989).
- [4] Y.-H. Qian, D. d’Humières, and P. Lallemand, Europhys. Lett. **17**, 479 (1992).
- [5] M. Atif, P. K. Kolluru, C. Thantapanally, and S. Ansumali, Phys. Rev. Lett. **119**, 240602 (2017).
- [6] M. Sbragaglia, R. Benzi, L. Biferale, S. Succi, and F. Toschi, Phys. Rev. Lett. **97**, 204503 (2006).
- [7] C. Kunert and J. Harting, Phys. Rev. Lett. **99**, 176001 (2007).
- [8] J. Hyväluoma and J. Harting, Phys. Rev. Lett. **100**, 246001 (2008).
- [9] R. Benzi, S. Chibarro, and S. Succi, Phys. Rev. Lett. **102**, 026002 (2009).
- [10] M. Thiébaud, Z. Shen, J. Harting, and C. Misbah, Phys. Rev. Lett. **112**, 238304 (2014).
- [11] C. K. Aidun and J. R. Clausen, Annu. Rev. Fluid. Mech. **42**, 439 (2010).
- [12] T. Krüger, H. Kusumaatmaja, A. Kuzmin, O. Shardt, G. Silva, and E. M. Viggen, *The Lattice Boltzmann Method* (Springer, Cham, 2017).
- [13] S. Succi, *The Lattice Boltzmann Equation* (Oxford University Press, Oxford, 2017).
- [14] Y.-H. Qian and S. A. Orszag, Europhys. Lett. **21**, 255 (1993).
- [15] F. J. Alexander, S. Chen, and J. D. Sterling, Phys. Rev. E **47**, R2249 (1993).
- [16] Z. Guo, C. Zheng, B. Shi, and T. S. Zhao, Phys. Rev. E **75**, 036704 (2007).
- [17] X. He, S. Chen, and G. D. Doolen, J. Comput. Phys. **146**, 282 (1998).
- [18] G. R. McNamara, A. L. Garcia, and B. J. Alder, J. Stat. Phys. **81**, 395 (1995).
- [19] X. Shan and X. He, Phys. Rev. Lett. **80**, 65 (1998).
- [20] S. Chapman and T. G. Cowling, *The Mathematical Theory of Non-Uniform Gases* (Cambridge University Press, Cambridge, 1961).
- [21] S. S. Chikatamarla and I. V. Karlin, Phys. Rev. Lett. **97**, 190601 (2006).
- [22] A. Krämer, K. Küllmer, D. Reith, W. Joppich, and H. Foyi, Phys. Rev. E **95**, 023305 (2017).
- [23] G. Di Ilio, B. Dorschner, G. Bella, S. Succi, and I. V. Karlin, J. Fluid Mech. **in press** (2018).
- [24] Y.-H. Qian and Y. Zhou, Europhys. Lett. **42**, 359 (1998).
- [25] G. Hazi and P. Kávrán, J. Phys. A **39**, 3127 (2006).
- [26] N. I. Prasianakis, I. V. Karlin, J. Mantzaras, and K. B. Boulouchos, Phys. Rev. E **79**, 066702 (2009).
- [27] S. Ansumali and I. V. Karlin, Phys. Rev. Lett. **95**, 260605 (2005).
- [28] X. B. Nie, X. W. Shan, and H. D. Chen, Europhys. Lett. **81**, 34005 (2008).
- [29] N. Frapolli, S. S. Chikatamarla, and I. V. Karlin, Phys. Rev. Lett. **117**, 010604 (2016).
- [30] X. Shan, J. Comput. Sci. **17**, 475 (2016).
- [31] C. Coreixas, G. Wissocq, G. Puigt, J.-P. Boussuge, and P. Sagaut, Phys. Rev. E **96**, 033306 (2017).
- [32] K. K. Mattila, P. C. Philippi, and L. A. Hegele Jr., Phys. Fluids **29**, 046103 (2017).
- [33] G. I. Taylor, Aero. Res. Commun. , 598 (1918).
- [34] Y. Inoue and Y. Hattori, J. Fluid Mech. **380**, 81 (1999).

Appendix A: Equilibrium

We consider the standard nine-velocity model, the D2Q9 lattice. The discrete speeds are constructed as a tensor product of two one-dimensional peculiar speeds, $c_i = i$, where $i = 0, \pm 1$. Discrete speeds in two-dimensions are

$$\mathbf{c}_{(i,j)} = (c_i, c_j)^\dagger, \quad (\text{A1})$$

where we have introduced two-dimensional indices in order to reflect the Cartesian frame instead of a more common single subscript. Thus, the discrete velocities are defined as

$$\mathbf{v}_{(i,j)} = \sqrt{\theta} \begin{pmatrix} c_i \\ c_j \end{pmatrix} + \begin{pmatrix} u_x \\ u_y \end{pmatrix}, \quad (\text{A2})$$

with reduced temperature $\theta = T/T_L$ and lattice temperature $T_L = 1/3$. Populations are labelled as well with two indices, $f_{(i,j)}$, corresponding to their respective velocities (A2). The local equilibrium populations are now conveniently expressed as the product of one-dimensional weights

$$f_{(i,j)}^{\text{eq}} = \rho W_{(i,j)} = \rho W_i W_j, \quad (\text{A3})$$

where

$$W_i = \begin{cases} 2/3, & \text{for } i = 0, \\ 1/6, & \text{otherwise.} \end{cases} \quad (\text{A4})$$

While the equilibrium populations are constant up to the proportionality to density, their moments

$$M_{mn}^{\text{eq}} = \rho \sum_{(i,j)} W_i W_j (\sqrt{\theta} c_i + u_x)^m (\sqrt{\theta} c_j + u_y)^n, \quad (\text{A5})$$

recover the pertinent Maxwell-Boltzmann moments up to the fourth order, $m + n = 4$, without error for any temperature and velocity.

Appendix B: Transfer Matrix

Populations $f_{(i,j)}^\lambda$ measured in the gauge λ , can be represented as linear combinations of 9 linearly independent moments,

$$M^\lambda = (M_{00}^\lambda, M_{10}^\lambda, M_{01}^\lambda, M_{11}^\lambda, M_{20}^\lambda, M_{02}^\lambda, M_{21}^\lambda, M_{12}^\lambda, M_{22}^\lambda)^\dagger, \quad (\text{B1})$$

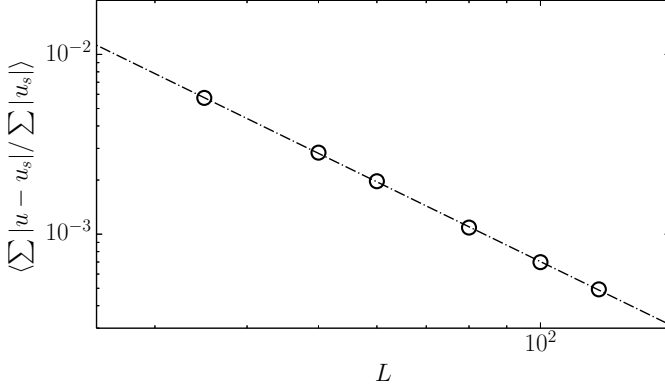


FIG. 5. Convergence rate of Green-Taylor vortex flow for grid resolutions $L \in [35, 120]$ and Reynolds number $\text{Re} = u_0 L / \nu = 50$. Symbols: relative error with respect to solution \mathbf{u}_s ; Line: second order convergence.

see also Eq. (2) in the main text, and \mathcal{M}_λ is the $Q \times Q$ matrix of the linear map between populations and moments,

$$\mathcal{M}_\lambda f^\lambda = M^\lambda. \quad (\text{B2})$$

Moments are invariant with respect to the gauge,

$$\mathcal{M}_{\lambda'} f^{\lambda'} = \mathcal{M}_\lambda f^\lambda, \quad (\text{B3})$$

and the transfer from gauge λ to λ' can be written in the following explicit form,

$$f_{(k,l)}^{\lambda'} = \omega(k)\omega(l) \sum_{i,j} g_x(i,k)g_y(j,l)f_{(i,j)}^\lambda, \quad (\text{B4})$$

where

$$g_\xi(i,j) = A_\xi^2(i) - B_\xi(i,j), \quad (\text{B5})$$

$$A_\xi(i) = (u'_\xi - u_\xi) / \sqrt{3} - i\sqrt{T}, \quad (\text{B6})$$

$$B_\xi(i,j) = \begin{cases} T, & \text{for } j = 0, \\ j\sqrt{T}A_\xi(i), & \text{otherwise,} \end{cases} \quad (\text{B7})$$

$$\omega(i) = \begin{cases} 1/T', & \text{for } i = 0, \\ -1/2T', & \text{otherwise.} \end{cases} \quad (\text{B8})$$

Formula (B4) only involves evaluation of a dot-product as opposed to numerically solving the linear system (B3).

Appendix C: Reconstruction

An equidistant rectilinear mesh with $\Delta x = 1$ is used for all simulations. Populations at off-grid locations are reconstructed using 3rd-order polynomial interpolation,

$$\tilde{f}_{(i,j)}^\lambda(\mathbf{x}, t) = \sum_{\substack{0 \leq m \leq 3 \\ 0 \leq n \leq 3}} a_{mn}(\mathbf{x}) f_{(i,j)}^\lambda((x_0 + n, y_0 + m), t), \quad (\text{C1})$$

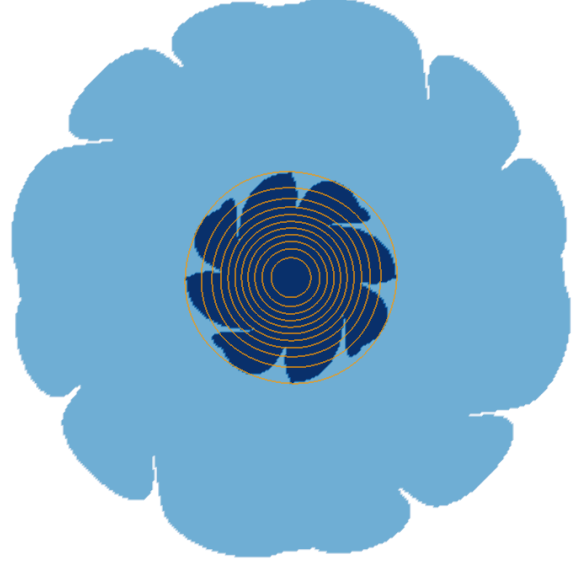


FIG. 6. Instantaneous recording of a standing vortex with rotation Mach number $\text{Ma}_v = 0.8$. Colors indicate number of iterations required for convergence of predictor-corrector scheme (white: 1, light blue: 2, dark blue: 3). Lines: density contours.

where the populations at integer collocation points $(x_0 + n, y_0 + m)$ are transformed to gauge λ using eq. (4) and a_{mn} are standard Lagrange polynomials,

$$a_{mn}(\mathbf{x}) = \prod_{\substack{0 \leq k \leq 3 \\ k \neq n}} \frac{(x - x_0) - k}{n - k} \prod_{\substack{0 \leq l \leq 3 \\ l \neq m}} \frac{(y - y_0) - l}{m - l}, \quad (\text{C2})$$

with respect to reference coordinate,

$$\mathbf{x}_0 = ([x] - 1, [y] - 1), \quad (\text{C3})$$

where the operation $\lfloor \varphi \rfloor$ rounds down to the largest integer value not greater than φ .

Appendix D: Convergence Order

Convergence with respect to grid resolution of the present method was tested using the well known periodic Green-Taylor vortex flow. Analytical solution of the flow field is given by

$$u_x(\mathbf{x}, t) = -(u_0/\sqrt{2}) \cos(kx) \sin(ky) \exp(-2\nu k^2 t), \quad (\text{D1})$$

$$u_y(\mathbf{x}, t) = (u_0/\sqrt{2}) \sin(kx) \cos(ky) \exp(-2\nu k^2 t), \quad (\text{D2})$$

with wave number $k = 2\pi/L$ and domain size L . In order to maintain incompressibility, a small characteristic Mach number $\text{Ma} = u_0/\sqrt{T} = 0.001$ was chosen and the simulation was run at isothermal conditions $T = 3T_L = 1$. Thus, the speed of sound is $\sqrt{3}$ times

larger than in a standard LBM simulation with the same lattice. Initial density was set to unity, $\rho_0 = 1$, and simulated flow field is compared to with respect to theoretical prediction. Fig. 5 shows the rate of convergence of the relative error averaged over a time period $[0.9t_h, 1.1t_h]$, where t_h is the half-decay time. The present scheme recovers second order of accuracy, which coincides with standard LBM and its semi-Lagrangian variant.

Appendix E: Predictor-Corrector Scheme

The number of predictor-corrector iterations depends on the flow and initial seed gauges, however, unique solution is found independent of the initial guess values. On average three iterations lead to convergence, which is

defined for iteration $n + 1$ of field ϕ by

$$|\phi_{n+1} - \phi_n| < \epsilon_{\text{abs}} + \epsilon_{\text{rel}}\phi_{n+1}, \quad (\text{E1})$$

where absolute tolerance $\epsilon_{\text{abs}} = 10^{-12}$ and relative tolerance $\epsilon_{\text{rel}} = 10^{-10}$ are used in the simulations. Convergence criterion (E1) must be separately fulfilled for $\phi = \{u_x, u_y, \sqrt{\theta}\}$. Fig. 6 shows the number of iterations at a particular instant in time for the standing vortex with vortex Mach number $\text{Ma}_v = 0.8$ (see main text for definition of the flow). Superimposed density contours indicate the center of the vortex. It is apparent that generally more iterations are needed in regions where the flow changes rapidly, and thus, initial seed values based on the previous time step (Eqs. (7) and (8) in the main text) are farther from the converged result. A maximum number of 5 iterations was recorded for high advection Mach numbers $\text{Ma}_a \approx 100$.